Composite Structures 291 (2022) 115609

Contents lists available at ScienceDirect

Composite Structures

journal homepage: www.elsevier.com/locate/compstruct

Free vibration analysis of functionally graded graphene nanocomposite beams partially in contact with fluid

Helong Wu [a,*], Yilin Li [a], Long Li [b], Sritawat Kitipornchai [c], Lin Wang [d], Jie Yang [e,*]

[a] College of Mechanical Engineering, Zhejiang University of Technology, Hangzhou 310014, China
[b] Institute of Mechanics, Chinese Academy of Sciences, Beijing 100190, China
[c] School of Civil Engineering, the University of Queensland, Brisbane, St Lucia 4072, Australia
[d] School of Aerospace Engineering, Huazhong University of Science and Technology, Wuhan 430074, China
[e] School of Engineering, RMIT University, PO Box 71, Bundoora, VIC 3083, Australia

ARTICLE INFO

Keywords:
Free vibration
Graphene nanocomposite
Functionally graded material
Fluid-structure interaction
Generalized differential quadrature

ABSTRACT

This paper presents the free vibration analysis of functionally graded graphene platelets reinforced composite (FG-GPLRC) beams partially in contact with fluid based on the first-order shear deformation theory (FSDT). By considering the 3D-random orientation of graphene platelets (GPLs), the 3D Halpin-Tsai model is introduced to calculate the elastic modulus of graphene nanocomposites. The fluid velocity potential and hydrodynamic loading are determined by virtue of variable separation method. The equations of motion are derived by using Hamilton's principle and the natural frequencies are determined by the multidomain generalized differential quadrature (GDQ) approach together with an iterative scheme. Parametric studies are carried out to evaluate the influences of GPL distribution pattern, weight fraction and dimension, fluid depth and density, beam geometry and end supports on the free vibration behaviour of FG-GPLRC beam-fluid interaction systems. Results show that the beam-fluid interaction reduces the fundamental frequency most, but it hardly affects the first order vibration mode.

1. Introduction

Graphene, a two-dimensional (2D) monolayer of carbon atoms, possesses extraordinary physical and mechanical properties [1], such as superior thermal conductivity [2], large surface area [3], exceptionally high elastic modulus and tensile strength [4]. These merits, along with nanoscale effect and interface chemistry [5], enable graphene and its derivatives desirable reinforcing materials for polymer composites. As a result, graphene/polymer nanocomposites have raised substantial interests among research and engineering communities [6–8], and such nanocomposites have found a variety of applications such as flexible electronics [9], biosensor technology [10], energy storage devices [11], as well as aerospace engineering [12].

One of the most recent advances in graphene nanocomposites is the functionally graded graphene nanocomposites, in which graphene or its derivatives are nonuniformly dispersed according to preset patterns so that the material properties are designable and can be tailored to meet multifunctional requirements [13–15]. Yang and his coauthors [16–19] demonstrated that the load capacity and vibration performance of nanocomposite beams and plates can be further enhanced via the gradient distribution of graphene platelets (GPLs) in the polymer matrix. Subsequently, mechanical behaviours of functionally graded graphene nanocomposite structures under various loading circumstances have been widely studied in the past few years, such as bending, buckling and vibration analyses of arches [20], beams [21,22], plates [23–25], and shells [26,27]. Readers can refer to the review paper by Zhao *et al.* [28] for more related works in this area.

In terms of vibration analysis, Feng *et al.* [29] studied the nonlinear free vibration of functionally graded GPL-reinforced composite (FG-GPLRC) beams and suggested that the natural frequencies are significantly increased by adding a very low content of GPLs. Song *et al.* [30] explored the same problem by additionally considering the effects of edge crack and elastic foundation and found that the edge crack considerably reduces the linear and nonlinear frequencies. Wang *et al.* [31] analysed the free vibration of functionally graded graphene-reinforced composite (FG-GRC) beams using a 2D elasticity theory and claimed that the effect of graphene distribution pattern is sensitive to the slenderness ratio. Shen *et al.* [32,33] employing a two-step perturbation

* Corresponding authors.
E-mail addresses: helongwu@zjut.edu.au (H. Wu), j.yang@rmit.edu.au (J. Yang).

https://doi.org/10.1016/j.compstruct.2022.115609
Received 12 January 2022; Received in revised form 2 April 2022; Accepted 16 April 2022
Available online 22 April 2022

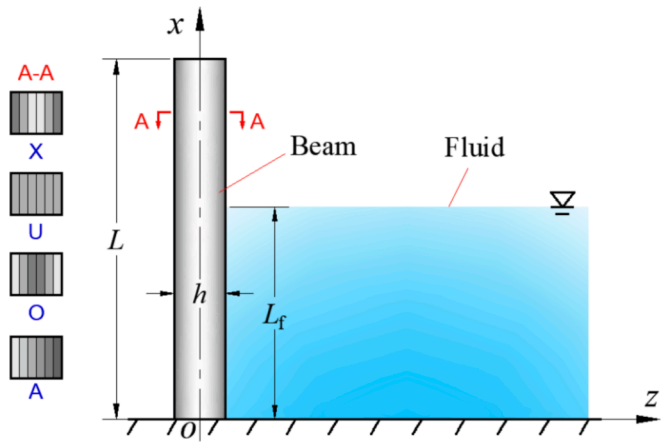

Fig. 1. Configuration and coordinate of an FG-GPLRC beam-fluid interaction system.

technique evaluated the nonlinear vibration of FG-GRC laminate beams and plates resting on elastic foundations in thermal environments. Their results show that the temperature elevation reduces fundamental frequency but increases the nonlinear-to-linear frequency ratio. This was further confirmed by Kiani [34] who examined the large amplitude vibration of FG-GRC plates under thermal loadings using a nonuniform rational B-spline (NURBS) based isogeometric finite element method. Reddy *et al.* [35] reported the free vibration analysis of FG-GPLRC plates based on the first order shear deformation theory (FSDT) and finite element approach. Qaderi *et al.* [36] extended this work by including the effect of temperature rise according to the higher order shear deformation theory (HSDT) and Navier solution.

Fluid-structure interaction is an essential consideration in the design of many engineering systems, such as automobile, aircraft, bridges, and marine vessels, where functionally graded graphene nanocomposites may be incorporated in the form of beam, plate, or shell owing to the advantages of high specific strength, excellent corrosion resistance and multifunctionality. There have been many researches on the fluid–structure interaction vibration of functionally graded material (FGM) structures. For example, Khorshidi and Bakhsheshy [37] studied the vibration of FGM plates partially in contact with a bounded fluid using the Rayleigh-Ritz method. Shahbaztabar and Ranji [38] presented a free vibration analysis of FGM plates on elastic foundation and coupled with fluid. Li *et al.* [39] investigated the free vibration of FGM beams with variable thickness based on the FSDT. The similar problem for variable thickness FGM circular columns was analysed by Houmat [40] using the three-dimensional (3D) elasticity theory. In these two studies, the beam and column are vertically submerged in an infinite fluid. Thinh *et al.* [41] dealt with the free vibration of FGM plates horizontally immersed in fluid. As far as the authors aware, no work has been reported on the fluid–structure interaction analysis of functionally graded nanocomposite structures. In addition, the aforementioned studies on FG-GPLRC and FG-GRC structures assumed that graphene nanofillers are 2D-randomly oriented or unidirectionally aligned in the polymer, which may lead to big discrepancy since in reality the graphene nanofillers are randomly oriented and dispersed in three dimensions (3D) due to the constraints of manufacture technology.

This paper aims to fill the research gap by assessing the interaction vibration of FG-GPLRC beams partially in contact with fluid. The 3D Halpin-Tsai model is introduced to take into account the 3D-random orientations of GPL nanofillers in the polymer. Governing equations of free vibration are derived by employing Hamilton's principle and then solved by the generalized differential quadrature (GDQ)-based iterative scheme, together with a multidomain technique that is used to overcome the discontinuity of computation domain. Parametric studies are carried out to highlight the influences of GPL and fluid parameters, such as GPL gradient pattern, concentration and dimension, fluid depth and density, on the free vibration behaviour of FG-GPLRC beam-fluid systems. Natural frequency results of FG-GPLRC beams in air and fully in contact with fluid are also presented for a comparison study.

2. Theoretical modelling

2.1. Beam-fluid interaction system

Let us consider an FG-GPLRC beam-fluid interaction system as illustrated in Fig. 1. The beam of length L and thickness h is partially in contact with the fluid of depth L_f. The origin o of the Cartesian coordinate system is located at the bottom centre of the beam ($z = 0$), and the $\times$ and z axes are along the vertical and horizontal directions, respectively.

The beam is composed of perfectly bonded GPLRC layers of equal thickness that are made from a mixture of GPL reinforcements and epoxy matrix. It is assumed that GPL reinforcements are randomly oriented and uniformly dispersed in each layer but the concentration changes in a layer-wise manner along the beam thickness. As shown in Fig. 1, four distribution patterns (X, U, O and A) are considered in present study and are characterized in order by [19].

$$\text{Pattern X}: V_{GPL}^{(k)} = 2V_{GPL}^{*}|2k - N_L - 1|/N_L \tag{1}$$

$$\text{Pattern U}: V_{GPL}^{(k)} = V_{GPL}^{*} \tag{2}$$

$$\text{Pattern O}: V_{GPL}^{(k)} = 2V_{GPL}^{*}(1 - |2k - N_L - 1|/N_L) \tag{3}$$

$$\text{Pattern A}: V_{GPL}^{(k)} = V_{GPL}^{*}(2k - 1)/N_L \tag{4}$$

where $V(k)$ GPL is the GPL volume fraction of the k^{th} layer ($k = 1, 2, \ldots, N_L$), and N_L is the total number of layers of the beam; V^* GPL is the total GPL volume fraction and is given by.

$$V_{GPL}^{*} = \frac{W_{GPL}}{W_{GPL} + (\rho_{GPL}/\rho_m)(1 - W_{GPL})} \tag{5}$$

in which W_{GPL} is the total GPL weight fraction, ρ_{GPL} and ρ_m are the mass densities of GPLs and matrix, respectively.

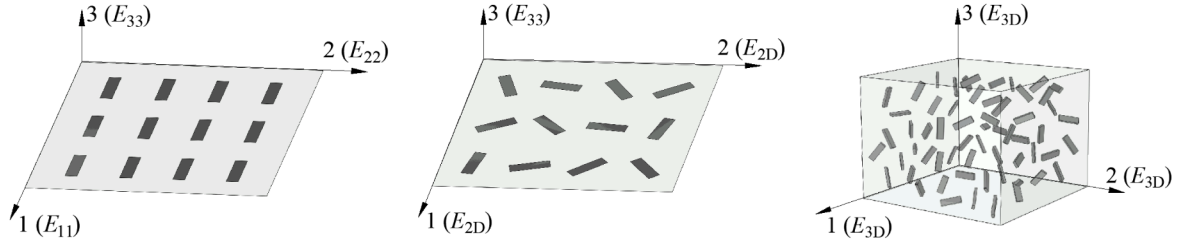

(a) Unidirectionally aligned (b) 2D-randomly oriented (c) 3D-randomly oriented

Fig. 2. Schematic diagram of nanocomposites with GPLs of different orientations.

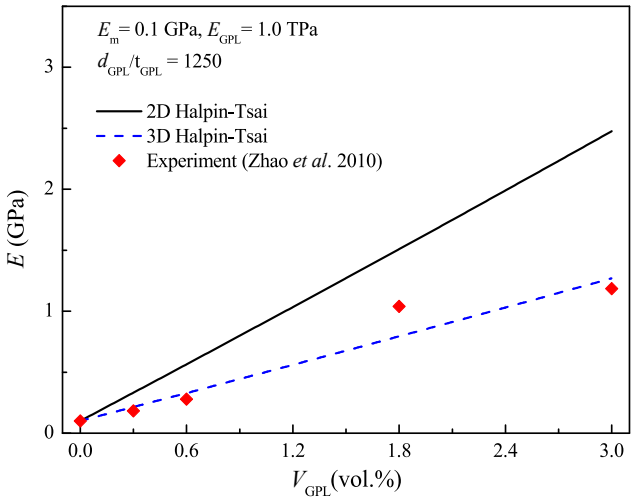

Fig. 3. Elastic modulus of graphene/polymer nanocomposites.

Table 1
Fundamental frequencies (Hz) of an X-GPLRC beam-fluid interaction system with varying numbers of grid points (W_{GPL} = 1.0%, L/h = 10, h = 0.1 m, ρ_f = 1000 kg/m^3).

N	C-F			C-C		
	$L_f/L = 0$	$L_f/L = 0.5$	$L_f/L = 1.0$	$L_f/L = 0$	$L_f/L = 0.5$	$L_f/L = 1.0$
5	42.95	43.86	24.93	269.3	203.2	124.8
7	45.49	44.35	26.06	266.9	205.9	121.4
9	45.46	44.36	26.09	267.0	205.8	120.4
11	45.46	44.36	26.10	267.0	205.7	119.9
13	45.46	44.36	26.12	267.0	205.7	119.7
15	45.46	44.37	26.14	267.0	205.7	119.5

Table 2
Comparison of fundamental frequency parameters ($\omega = \Omega L\sqrt{I_{10}/A_{110}}$) for FG-CNTRC beams in air (L/h = 25, V_{cn}^{*} = 0.17).

CNTRC	H-H		C-C	
	Present	Wu et al. [50]	Present	Wu et al. [50]
X	0.8729	0.8729	1.4751	1.4750
U	0.7387	0.7386	1.3326	1.3325
O	0.5474	0.5474	1.0833	1.0834

Table 3
Comparison of fundamental frequency parameters ($\omega = \sqrt{\overline{\omega}}$, $\overline{\omega} = \Omega L^2\sqrt{\rho_s h/EI}$) for a cantilever isotropic homogeneous beam-water interaction system.

L_f/L	Source	$\rho_f L/\rho_s h$		
		5	8	10
0.5	Present	1.8564	1.8519	1.8475
	Xing *et al.* [51]	1.8620	1.8544	1.8493
	Eftekhari and Jafari [52]	1.8620	1.8543	1.8492
0.8	Present	1.7243	1.6616	1.6244
	Xing *et al.* [51]	1.7311	1.6654	1.6275
	Eftekhari and Jafari [52]	1.7309	1.6651	1.6273
1.0	Present	1.5336	1.4308	1.3777
	Xing *et al.* [51]	1.5391	1.4340	1.3801
	Eftekhari and Jafari [52]	—	—	—

2.2. 3D Halpin-Tsai model

Previous studies assumed that graphene nanofillers are either unidirectionally aligned or 2D-randomly oriented and dispersed in the matrix, as shown in Fig. 2a and 2b. However, this is not often the real case and the nanofillers are 3D-randomly oriented and dispersed (Fig. 2c) because of the constrains of manufacture technology. As a result, the 2D Halpin-Tsai model often overestimates the elastic modulus of graphene nanocomposites when compared to the experimental test. In this section, the 3D Halpin-Tsai model is introduced to evaluate the elastic modulus of nanocomposites with 3D-randomly oriented GPLs.

To begin with, we consider the composite with unidirectionally aligned GPLs, as illustrated in Fig. 2(a). The elastic modulus of unidirectional composites can be predicted by the Halpin-Tsai equation as [42].

$$E_{ii} = \frac{1+\xi_i\eta_i V_{GPL}}{1-\eta_i V_{GPL}}E_m, \eta_i = \frac{E_{GPL}-E_m}{E_{GPL}+\xi_i E_m}, \quad (i = 1, 2, 3) \tag{6}$$

where E_m and E_{GPL} are elastic moduli of the matrix and GPLs, respectively. ξ_i is the shape factor depending on the nanofillers' geometry and loading direction. By comparing with the Mori-Tanaka theory, van Es [43] suggested that the Halpin-Tsai equation (6) should be used for platelet fillers with the following shape factors:

$$\xi_1 = 2a_{GPL}/3t_{GPL} \text{for } E_{11}, \quad \xi_2 = 2b_{GPL}/3t_{GPL} \text{ for } E_{22}, \quad \xi_3 = 2 \text{ for } E_{33} \tag{7}$$

in which E_{11} and E_{22} are the in-plane elastic moduli, and E_{33} the out-plane modulus of unidirectional composites, respectively. a_{GPL}, b_{GPL} and t_{GPL} are the length, width and thickness of GPLs in order.

To simulate the 2D-random composite, the unidirectional composite in Fig. 2(a) is randomised around the 3-axis. As a result, the orientations of GPLs are uniformly distributed between 0° and 90° in the lamina as indicated in Fig. 2(b). Laminate theory shows that the in-plane elastic modulus of composites with 2D-randomly oriented fillers can be estimated by [44,45].

$$E_{2D} = 0.375E_{11} + 0.625E_{22} \tag{8}$$

while the out-plane elastic modulus E_{33} is not changed after the randomising procedure around the 3-axis. It should be noted that for a correct calculation E_{11} in Eq. (8) is always taken to be the highest elastic modulus of the sheet [43].

To obtain the 3D-random composite, the 2D-random composite is repeatedly randomised around other axes by turns. After several randomising steps, the elastic modulus of composites with 3D-randomly oriented GPLs can be calculated by repeatedly using the 2D Halpin-Tsai equation (8). To illustrate the calculation, a few steps of the randomising procedure starting with the unidirectional composite are presented as follows:

1st step, randomise around 3-axis:

$$E_{33}^{(1)} = E_{33}$$

$$E_{11}^{(1)} = E_{22}^{(1)} = 0.375E_{11} + 0.625E_{22}$$

2nd step, randomise around 2-axis:

$$E_{22}^{(2)} = E_{22}^{(1)} = 0.375E_{11} + 0.625E_{22}$$

$$E_{11}^{(2)} = E_{33}^{(2)} = 0.375E_{11}^{(1)} + 0.625E_{33}^{(1)} = 0.141E_{11} + 0.234E_{22} + 0.625E_{33}$$

3rd step, randomise around 1-axis:

$$E_{11}^{(3)} = E_{11}^{(2)} = 0.141E_{11} + 0.234E_{22} + 0.625E_{33}$$

$$E_{22}^{(3)} = E_{33}^{(3)} = 0.375E_{22}^{(2)} + 0.625E_{33}^{(2)} = 0.229E_{11} + 0.381E_{22} + 0.391E_{33}$$

4th step, randomise around 3-axis:

$$E_{33}^{(4)} = E_{33}^{(3)} = 0.229E_{11} + 0.381E_{22} + 0.391E_{33}$$

$$E_{11}^{(4)} = E_{22}^{(4)} = 0.375E_{11}^{(3)} + 0.625E_{22}^{(3)} = 0.174E_{11} + 0.289E_{22} + 0.537E_{33}$$

Table 4
Fundamental frequencies (Hz) of C-F FG-GPLRC beams with different GPL distribution patterns and weight fractions in air and fully in contact with fluid ($L/h = 10$, $\rho_f = 1000$ kg/m^3).

W_{GPL}	In air				Fully in contact with fluid			
	X	U	A	O	X	U	A	O
0.0%	26.92	26.92	26.92	26.92	15.48	15.48	15.48	15.48
0.5%	37.34	34.34	33.51	31.04	21.47	19.75	19.27	17.86
1.0%	45.46	40.44	38.37	34.68	26.12	23.25	22.07	19.95
1.5%	52.35	45.74	42.48	37.98	30.07	26.29	24.43	21.85

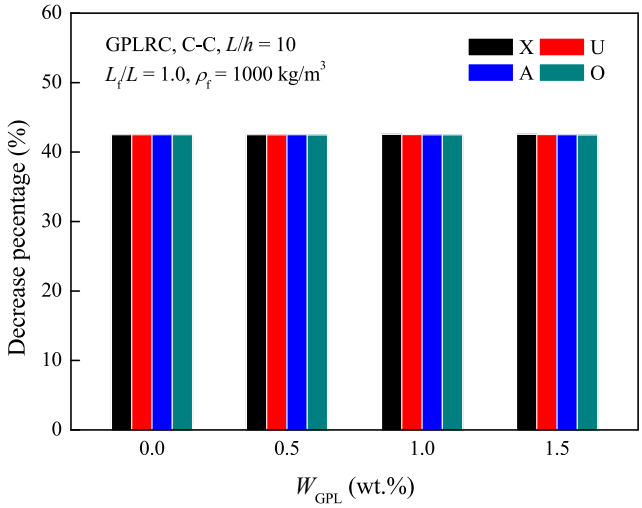

Fig. 4. Decrease percentage of the fundamental frequency of FG-GPLRC beam-fluid systems.

Table 5
First three natural frequencies (Hz) of X-GPLRC beams with different boundary conditions in air and fully in contact with fluid ($W_{GPL} = 1.0\%$, $L/h = 10$, $\rho_f = 1000$ kg/m^3).

BCs	In air			Fully in contact with fluid		
	$\Omega^a{}_1$	$\Omega^a{}_2$	$\Omega^a{}_3$	$\Omega^f{}_1$	$\Omega^f{}_2$	$\Omega^f{}_3$
C-F	45.46	268.4	693.6	26.12	154.9	470.8
C-H	190.9	572.1	1087	87.81	354.4	768.5
C-C	267.0	669.3	1187	119.7	374.5	858.6

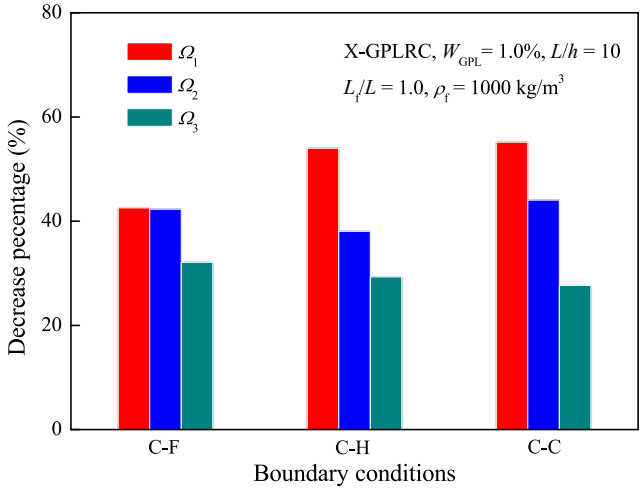

Fig. 5. Decrease percentage of the first three natural frequencies of the X-GPLRC beam-fluid system.

5th step, randomise around 2-axis:

$$E_{22}^{(5)} = E_{22}^{(4)} = 0.174E_{11} + 0.289E_{22} + 0.537E_{33}$$

$$E_{11}^{(5)} = E_{33}^{(5)} = 0.375E_{33}^{(4)} + 0.625E_{11}^{(4)} = 0.194E_{11} + 0.324E_{22} + 0.482E_{33}$$

…….It can be found that after 12 steps the elastic moduli in all three directions converge to the same value as

$$E_{11}^{(12)} = E_{22}^{(12)} = E_{33}^{(12)} = E_{3D} = 0.184E_{11} + 0.306E_{22} + 0.510E_{33} \quad (9)$$

For the composite filled with circular fibres ($E_{22} = E_{33}$), the above equation is reduced to

$$E_{3D} = 0.184E_{11} + 0.816E_{22} \quad (10)$$

while for that reinforced with circular GPLs ($E_{11} = E_{22}$), Eq. (9) can be rewritten as

$$E_{3D} = 0.49E_{11} + 0.51E_{33} \quad (11)$$

Accordingly, the shape factors for circular GPLs can be expressed as

$$\xi_1 = 2d_{GPL}/3t_{GPL} \text{ for } E_{11}, \quad \xi_2 = 2d_{GPL}/3t_{GPL} \text{ for } E_{22}, \quad \xi_3 = 2 \text{ for } E_{33} \quad (12)$$

where d_{GPL} is the average diameter of circular GPLs.

Fig. 3 shows the elastic moduli of graphene/polymer nanocomposites with different sources. The material properties used in this example are $E_m = 0.1$ GPa, $E_{GPL} = 1.0$ TPa, $d_{GPL} = 1$ μm, $t_{GPL} = 0.8$ nm. It is seen that the 2D Halpin-Tsai equation dramatically overestimates the elastic modulus of graphene/polymer nanocomposites, while the 3D Halpin-Tsai predictions agree well with the experimental data of Zhao *et al.* [46]. This indicates that graphene nanofillers are more inclined to be 3D-randomly dispersed in the polymer matrix, rather than 2D-randomly oriented.

The other material properties of GPLRCs are calculated by the rule of mixture as.

$$\nu = \nu_m V_m + \nu_{GPL} V_{GPL} \quad (13)$$

$$\rho = \rho_m V_m + \rho_{GPL} V_{GPL} \quad (14)$$

in which ν and ρ denote the Poisson's ratio and mass density, with subscripts "GPL" and "m" representing GPL and matrix, respectively. V_m is the volume fraction of the matrix and is given by

$$V_m = 1 - V_{GPL} \quad (15)$$

2.3. Hydrodynamic functions

It is assumed that the fluid is incompressible, inviscid and irrotational, such that the fluid motion is governed by the Laplace equation:

$$\frac{\partial^2 \Phi}{\partial x^2} + \frac{\partial^2 \Phi}{\partial z^2} = 0 \quad (16)$$

where $\Phi(x, z, t)$ is the fluid velocity potential and t the time. By using the method of variable separation, the velocity potential can be expressed as

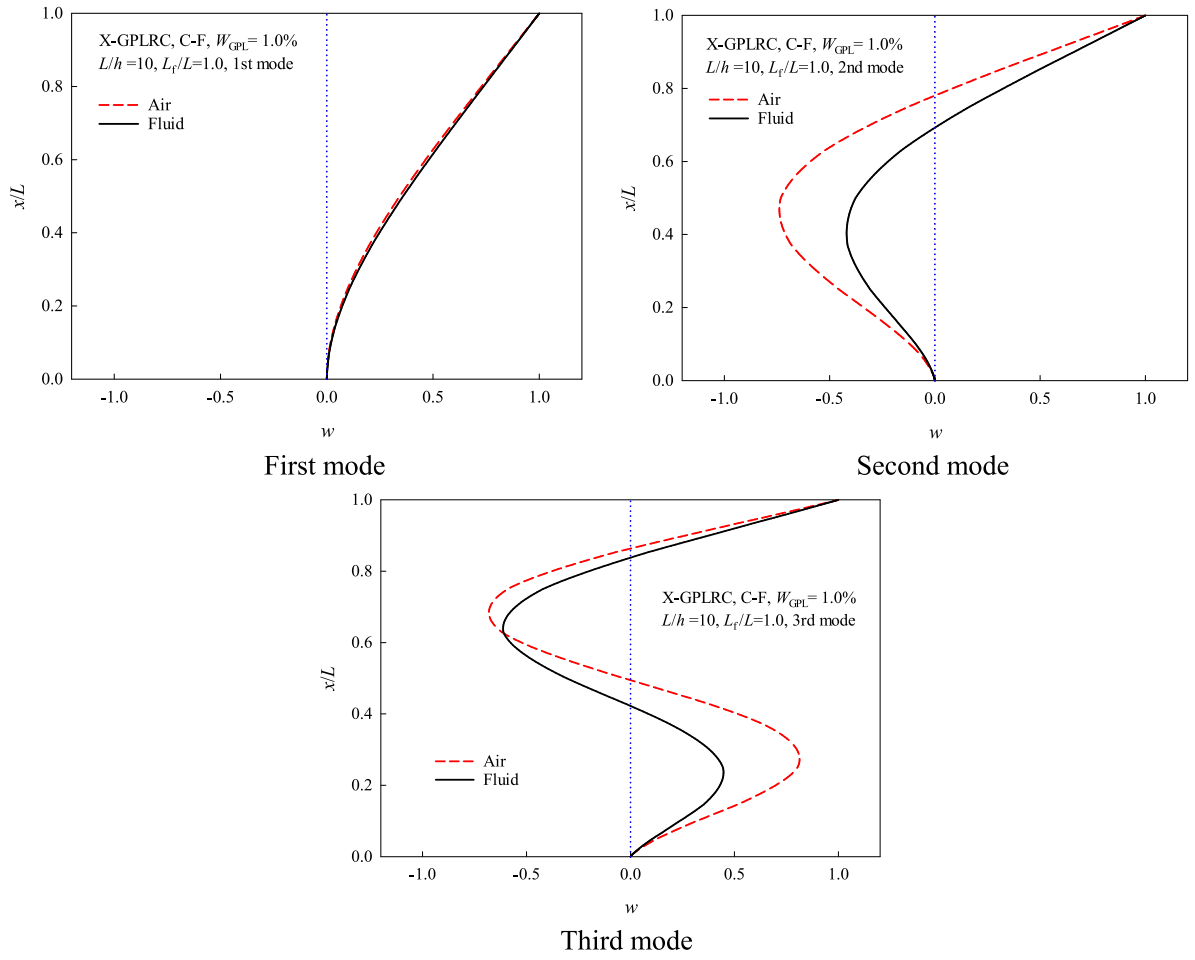

Fig. 6. Vibration mode shapes of C-F X-GPLRC beams in air and fully in contact with fluid.

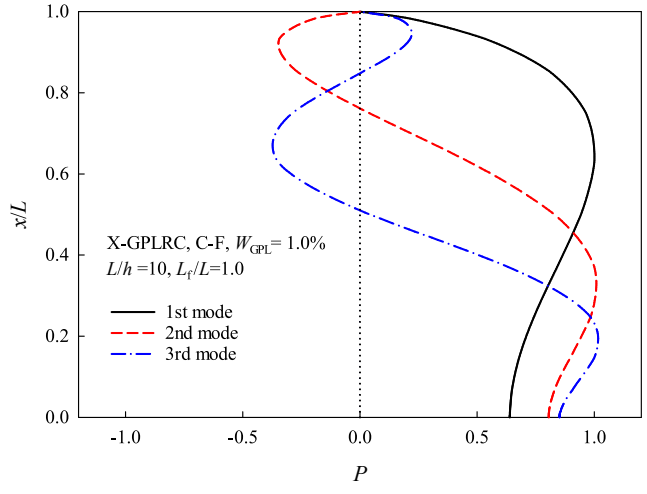

Fig. 7. Hydrodynamic pressure of the C-F X-GPLRC beam fully in contact with fluid.

$$\Phi = \Phi_x(x)\Phi_z(z)\dot{T}(t) \tag{17}$$

in which the overdot denotes the differential with respect to time t.

For the flow analysis, 1) the influence of free surface wave disturbance is neglected; 2) the velocity potential vanishes at infinity; 3) there is no vertical motion on the bottom of fluid; 4) the transverse components of velocity of the beam and fluid are the same on the beam-fluid interaction interface. This implies that the velocity potential must satisfy the following boundary conditions:

$$\Phi|_{x=L_f} = 0,\ \Phi|_{z=+\infty} = 0,\ \left.\frac{\partial\Phi}{\partial x}\right|_{x=0} = 0,\ \left.\frac{\partial\Phi}{\partial z}\right|_{z=h/2} = \frac{\partial W}{\partial t}, \tag{18}$$

in which $W(x, t) = w(x)T(t)$ is the vibrational deflection of the beam. By substituting the above boundary conditions and Eq. (17) into Eq. (16), we can obtain the expression of fluid velocity potential as

$$\Phi = \sum_{n=1}^{\infty} a_n \cos(\lambda x) e^{-\lambda z} \cdot \dot{T}(t) \tag{19}$$

where the coefficients a_n and λ are given by

$$a_n = -\frac{2e^{kh/2}}{kL_f}\int_0^{L_f} w(x)\cos(\lambda x)\mathrm{d}x \tag{20}$$

$$\lambda = \frac{(2n-1)\pi}{2L_f},\quad (n = 1,\ 2,\ 3,\ \ldots). \tag{21}$$

The hydrodynamic pressure due to the fluid motion, $P(x, z, t)$, is then determined by the Bernoulli's equation as.

$$P(x, z, t) = -\rho_f \frac{\partial\Phi}{\partial t} \tag{22}$$

in which ρ_f is the mass density of the fluid. By virtue of Eqs. (19)-(21), the above equation is rewritten as

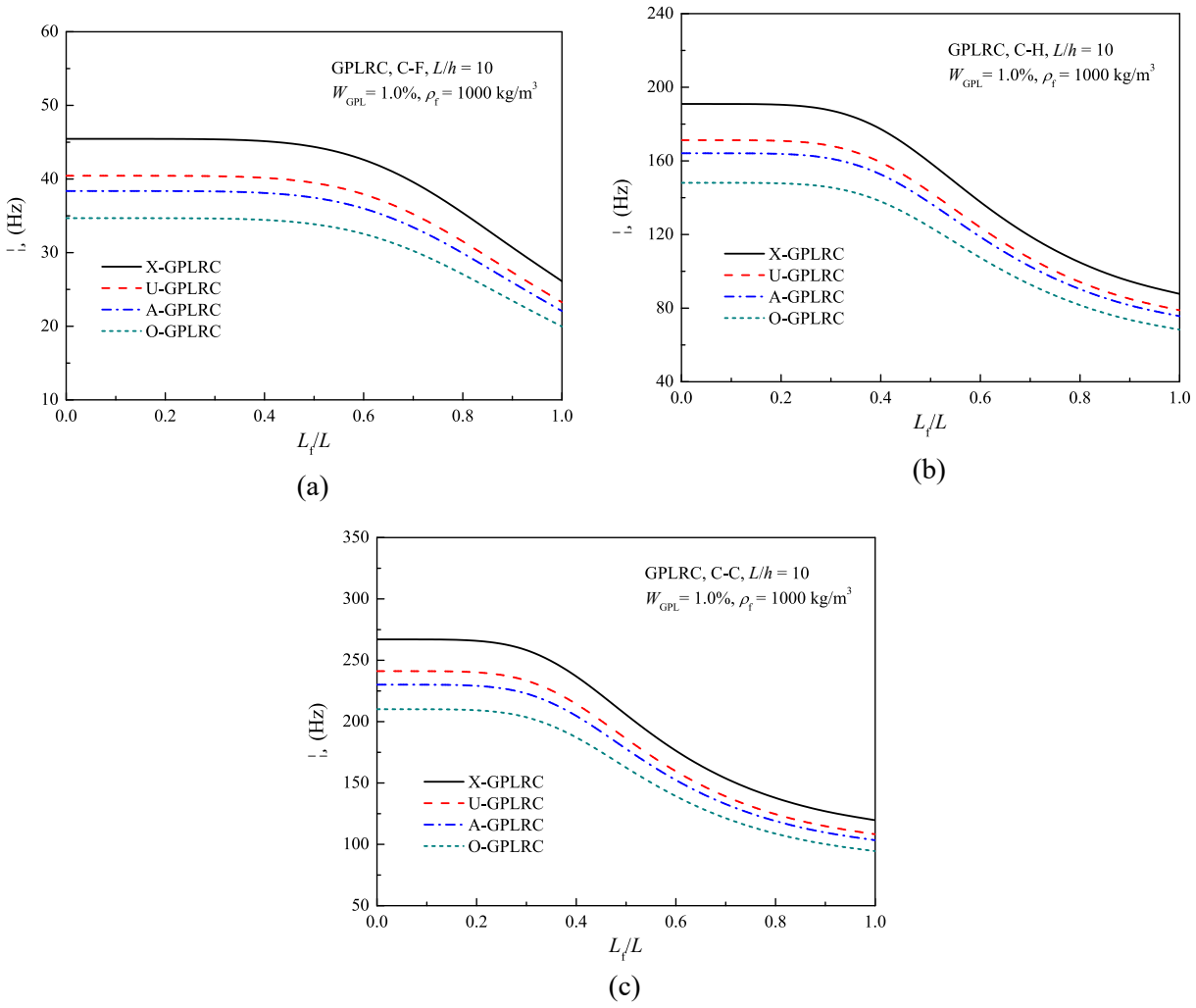

Fig. 8. Effect of GPL distribution pattern on the fundamental frequency of FG-GPLRC beam-fluid interaction systems: (a) C-F; (b) C-H; (c) C-C.

$$P(x,z,t)=\frac{4\rho_f}{\pi}\sum_{n=1}^{\infty}\frac{1}{2n-1}\cos\frac{(2n-1)\pi x}{2L_f}\int_0^{L_f}w(x)\cos\frac{(2n-1)\pi x}{2L_f}\mathrm{dx}\cdot\ddot{T}(t) \tag{23}$$

2.4. Governing equations

Let $\overline{U}$ and $\overline{W}$ denote the displacements of the beam along the × and z directions, respectively. According to the FSDT, the displacement field of the beam is of the following form:

$$\overline{U}(x,z,t)=U(x)+z\psi(x,t),\ \overline{W}(x,\ z,\ t)=W(x,\ t), \tag{25}$$

in which U and W are displacement components on the mid-plane ($z=0$) along x- and y-axes; ψ is the transverse normal rotation about the x-axis. The linear strain components associated with the displacements are then given by

$$\varepsilon_{xx}=\frac{\partial U}{\partial x}+z\frac{\partial\psi}{\partial x},\qquad \gamma_{xz}=\frac{\partial W}{\partial x}+\psi. \tag{26}$$

The governing equations of the beam-fluid interaction system can be obtained by employing the Hamilton's principle:

$$\int_{t_1}^{t_2}\delta(\Pi_S-\Pi_K-\Pi_W)\mathrm{dt}=0 \tag{27}$$

where the strain energy Π_S, kinetic energy Π_K, and the work Π_W done by the hydrodynamic load are formulated as follows:

$$\begin{aligned}\Pi_S&=\frac{1}{2}\int_0^L\int_{-h/2}^{h/2}\left(Q_{11}\varepsilon_{xx}^2+Q_{55}\gamma_{xz}^2\right)\mathrm{dzdx}\\&=\frac{1}{2}\int_0^L\int_{-h/2}^{h/2}\left[Q_{11}\left(\frac{\partial U}{\partial x}+z\frac{\partial\psi}{\partial x}\right)^2+Q_{55}\left(\frac{\partial W}{\partial x}+\psi\right)^2\right]\mathrm{dzdx}\end{aligned} \tag{28}$$

$$\begin{aligned}\Pi_K&=\frac{1}{2}\int_0^L\int_{-h/2}^{h/2}\rho\left[\left(\frac{\partial\overline{U}}{\partial t}\right)^2+\left(\frac{\partial\overline{W}}{\partial t}\right)^2\right]\mathrm{dzdx}=\frac{1}{2}\int_0^L\\&\quad\times\int_{-h/2}^{h/2}\rho\left[\left(\frac{\partial U}{\partial t}+z\frac{\partial\psi}{\partial t}\right)^2+\left(\frac{\partial W}{\partial t}\right)^2\right]\mathrm{dzdx}\end{aligned} \tag{29}$$

$$\Pi_W=-\int_0^{L_f}P\cdot W\mathrm{dx} \tag{30}$$

Substituting Eqs. (28)-(30) into Eq. (27) and integrating by parts over the beam thickness, the governing equations are then derived by setting the coefficients of δU, δW and $\delta\psi$ to zero separately and expressed in terms of displacements as

$$A_{11}\frac{\partial^2U}{\partial x^2}+B_{11}\frac{\partial^2\psi}{\partial x^2}=I_1\frac{\partial^2U}{\partial t^2}+I_2\frac{\partial^2\psi}{\partial t^2} \tag{31}$$

$$A_{55}\left(\frac{\partial^2W}{\partial x^2}+\frac{\partial\psi}{\partial x}\right)=\left(I_1+I_f\right)\frac{\partial^2W}{\partial t^2} \tag{32}$$

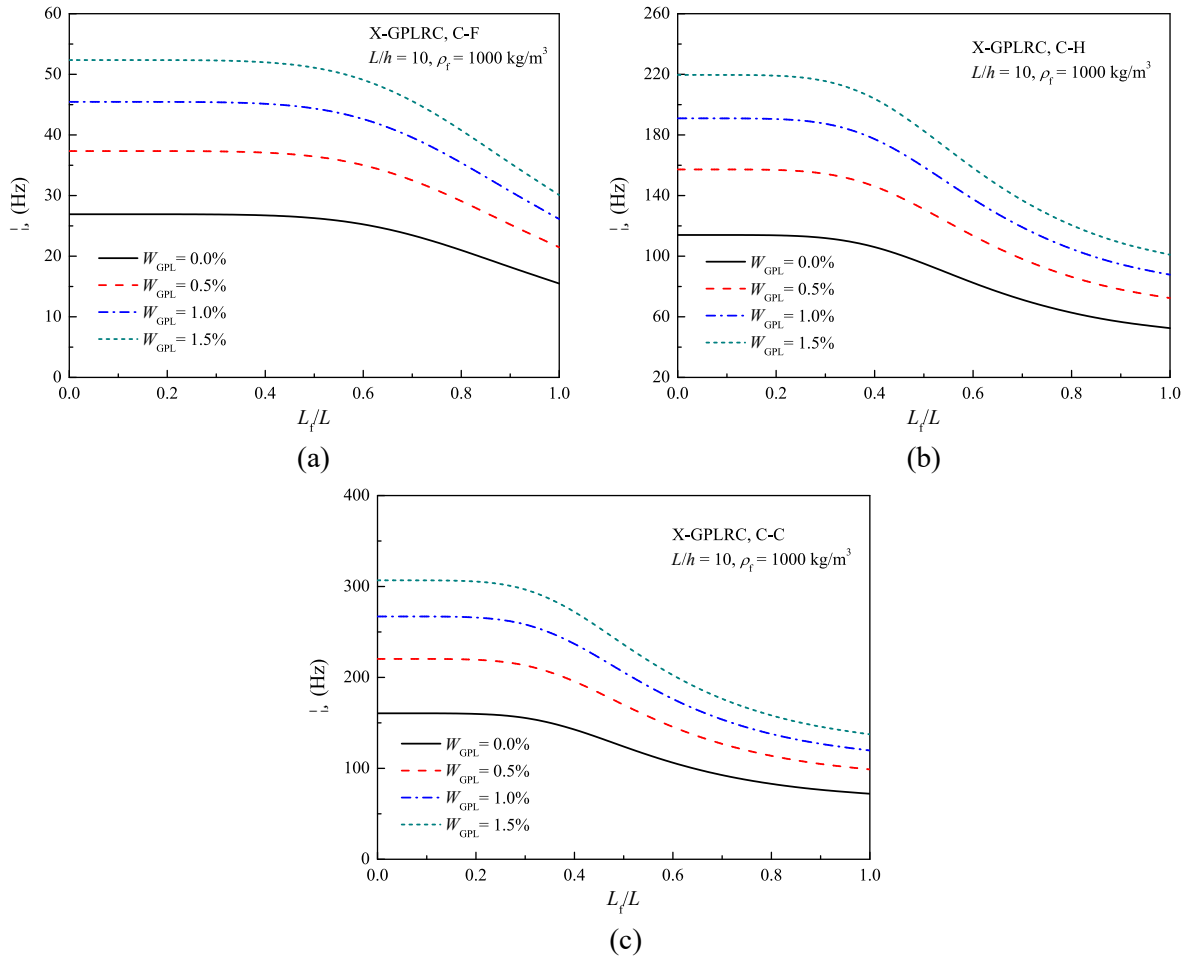

Fig. 9. Effect of GPL weight fraction on the fundamental frequency of FG-GPLRC beam-fluid interaction systems: (a) C-F; (b) C-H; (c) C-C.

$$B_{11}\frac{\partial^2 U}{\partial x^2}+D_{11}\frac{\partial^2 \psi}{\partial x^2}-A_{55}\left(\frac{\partial W}{\partial x}+\psi\right)=I_2\frac{\partial^2 U}{\partial t^2}+I_3\frac{\partial^2 \psi}{\partial t^2} \tag{33}$$

Given that the k^{th} layer of the beam is located between $z = z_k$ and $z = z_{k+1}$ along the z-axis. The stiffness elements A_{ij}, D_{ij} and inertia related terms I_i in the above equations are defined as

$$\{A_{11},\ B_{11},\ D_{11}\}=\int_{-h/2}^{h/2} Q_{11}\{1,\ z,\ z^2\}\mathrm{dz}=\sum_{k=1}^{N_L}\int_{z_k}^{z_{k+1}} Q_{ij}^{(k)}\{1,\ z,\ z^2\}\mathrm{dz} \tag{34}$$

$$A_{55}=\kappa\int_{-h/2}^{h/2} Q_{55}\mathrm{dz}=\kappa\sum_{k=1}^{N_L}\int_{z_k}^{z_{k+1}} Q_{55}^{(k)}\mathrm{dz} \tag{35}$$

$$\{I_1,\ I_2,\ I_3\}=\int_{-h/2}^{h/2}\rho\{1,\ z,\ z^2\}\mathrm{dz}=\sum_{k=1}^{N_L}\int_{z_k}^{z_{k+1}}\rho^{(k)}\{1,\ z,\ z^2\}\mathrm{dz} \tag{36}$$

in which κ is the shear correction factor having a value of 5/6; the elastic stiffness components Q_{ij} are given by

$$Q_{11}=\frac{E}{1-\nu^2},\quad Q_{55}=\frac{E}{2(1+\nu)}. \tag{37}$$

I_f in Eq. (32) is the added inertia due to the fluid motion and is formulated as

$$I_f(x)=\frac{4\rho_f}{\pi w(x)}\sum_{n=1}^{\infty}\frac{1}{2n-1}\cos\frac{(2n-1)\pi x}{2L_f}\int_0^{L_f} w(x)\cos\frac{(2n-1)\pi x}{2L_f}\mathrm{dx} \tag{38}$$

Three different end supports are considered in the present analysis, namely clamped (C), hinged (H), and free (F). The corresponding boundary conditions can be written as

$$\text{Clamped}:\ U=0,\ W=0,\ \psi=0; \tag{39}$$

$$\text{Hinged}:\ U=0, W=0, B_{11}\frac{\partial U}{\partial x}+D_{11}\frac{\partial \psi}{\partial x}=0$$

$$\text{Free}:\ A_{11}\frac{\partial U}{\partial x}+B_{11}\frac{\partial \psi}{\partial x}=0,\ A_{55}\left(\frac{\partial W}{\partial x}+\psi\right)=0,\ B_{11}\frac{\partial U}{\partial x}+D_{11}\frac{\partial \psi}{\partial x}=0. \tag{41}$$

3. Solution procedure

The GDQ method is a highly efficient numerical approach which can obtain accurate numerical solutions but requires a very small number of grid points [47,48]. It approximates the spatial derivative of a function at a given grid point as the weighted linear sum of the function values at all grid points generated in the whole domain. In this manner, the differential equations are converted to a set of algebraic equations that can then be easily solved by a computer program.

According to the GDQ approximation, the displacement components and their m^{th} derivatives with respect to × can be discretised as.

$$\{U,\ W,\ \psi\}\,|_{x=x_i}=\sum_{j=1}^{N} l_j(x_i)\{U_j,\ W_j,\ \psi_j\},\ \frac{\partial^m}{\partial x^m}\{U,\ W,\ \psi\}\Big|_{x=x_i}$$
$$=\sum_{j=1}^{N} C_{ij}^{(m)}\{U_j,\ W_j,\ \psi_j\} \tag{42}$$

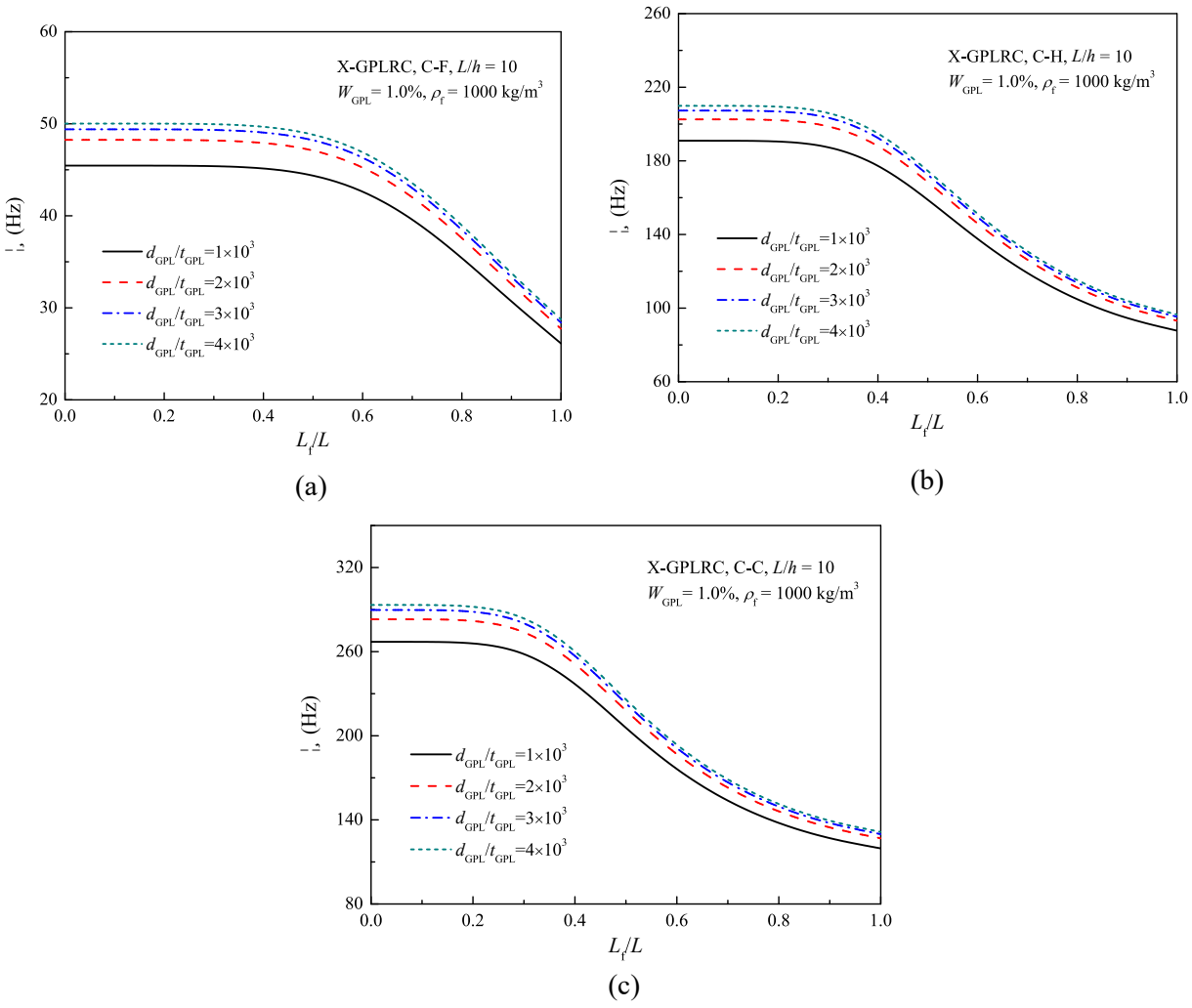

Fig. 10. Effect of GPL geometry on the fundamental frequency of FG-GPLRC beam-fluid interaction systems: (a) C-F; (b) C-H; (c) C-C.

in which $l_j(x)$ is the Lagrange interpolation polynomial; $\{U_j, W_j, \psi_j\}$ are the values of $\{U, W, \psi\}$ at $\times = x_j$; N is the number of grid points in the $\times$ direction. $C(m)$ ij are the weighting coefficients of the m^{th} partial derivatives to be determined by the following recursive formulae [49]:

$$C_{ij}^{(1)} = \begin{cases} \dfrac{R(x_i)}{(x_i - x_j)R(x_j)}, & \text{when j} \neq \text{i} \\ \displaystyle\sum_{k=1,k\neq i}^{N} C_{ik}^{(1)}, & \text{when j} = \text{i} \end{cases} \tag{43}$$

$$C_{ij}^{(m)} = \begin{cases} m\cdot\left(C_{ii}^{(m-1)}\cdot C_{ij}^{(1)} - \dfrac{C_{ij}^{(m-1)}}{x_i - x_j}\right), & \text{when j} \neq \text{i} \\ \displaystyle\sum_{k=1,k\neq i}^{N} C_{ik}^{(m)}, & \text{when j} = \text{i} \end{cases} \tag{44}$$

where $i, j = 1, 2, \ldots, N$, and $m = 2, 3, \ldots, N\text{-}1$. Besides,

$$R(x_i) = \prod_{j=1,j\neq i}^{N} (x_i - x_j) \tag{45}$$

As shown in Fig. 1, the beam is divided by the fluid free surface into two parts, namely the fluid (lower) and air (upper) ones. In this case, the GDQ method cannot be applied directly due to the discontinuity of computational domain. This difficulty can be overcome by use of a multidomain technique. The basic ideal of this approach is to decompose the whole computational domain into several subdomains, and then in each single subdomain the GDQ approximation is applied to discretise the derivatives. To this end, the following grid point distributions are used for the two subdomains:

$$x_i = \begin{cases} \dfrac{L_f}{2}\left[1 - \cos\dfrac{\pi(i-1)}{N_1 - 1}\right], & \text{for the fluid subdomain}: 0 \leqslant x \leqslant L_f,\ i = 1, 2, \ldots, N_1; \\ L_f + \dfrac{L - L_f}{2}\left[1 - \cos\dfrac{\pi(i - N_1 - 1)}{N_2 - 1}\right], & \text{for the air subdomain}: L_f \leqslant x \leqslant L,\ i = N_1 + 1, N_1 + 2, \ldots, N_1 + N_2. \end{cases} \tag{46}$$

Applying the GDQ approximation (42), the governing equations (31)-(33) can be discretised as.

$$A_{11}\sum_{j=1}^{N_1} C_{ij}^{(2)}U_j + B_{11}\sum_{j=1}^{N_1} C_{ij}^{(2)}\psi_j = I_1\ddot{U}_i + I_2\ddot{\psi}_i \tag{47}$$

$$A_{55}\left(\sum_{j=1}^{N_1} C_{ij}^{(2)}W_j + \sum_{j=1}^{N_1} C_{ij}^{(1)}\psi_j\right) = \left[I_1 + I_f(x_i)\right]\ddot{W}_i \tag{48}$$

$$B_{11}\sum_{j=1}^{N_1} C_{ij}^{(2)}U_j + D_{11}\sum_{j=1}^{N_1} C_{ij}^{(2)}\psi_j - A_{55}\left(\sum_{j=1}^{N_1} C_{ij}^{(1)}W_j + \psi_i\right) = I_2\ddot{U}_i + I_3\ddot{\psi}_i \tag{49}$$

for the fluid subdomain ($i = 1, 2, \ldots, N_1$), and

$$A_{11}\sum_{j=N_1+1}^{N_T} C_{ij}^{(2)}U_j + B_{11}\sum_{j=N_1+1}^{N_T} C_{ij}^{(2)}\psi_j = I_1\ddot{U}_i + I_2\ddot{\psi}_i \tag{50}$$

$$A_{55}\left(\sum_{j=N_1+1}^{N_T} C_{ij}^{(2)}W_j + \sum_{j=N_1+1}^{N_T} C_{ij}^{(1)}\psi_j\right) = I_1\ddot{W}_i \tag{51}$$

$$B_{11}\sum_{j=N_1+1}^{N_T} C_{ij}^{(2)}U_j + D_{11}\sum_{j=N_1+1}^{N_T} C_{ij}^{(2)}\psi_j - A_{55}\left(\sum_{j=N_1+1}^{N_T} C_{ij}^{(1)}W_j + \psi_i\right) = I_2\ddot{U}_i + I_3\ddot{\psi}_i \tag{52}$$

for the air subdomain ($i = N_1 + 1, N_1 + 2, \ldots, N_T$), in which $N_T = N_1 + N_2$ is the total number of grid points in the whole computational domain. $\{\ddot{U}_i, \ddot{W}_i, \ddot{\psi}_i\}$ are the values of second order derivatives of $\{U, W, \psi\}$ with respect to time t at $\times = x_i$. Note that the added inertia term I_f vanishes for the air subdomain. Similarly, we can discretise the boundary conditions (39)-(41) at the beam ends as

$$\text{Clamped}: \begin{cases} U_1 = W_1 = \psi_1 = 0 & \text{at } x = x_1, \\ U_{N_T} = W_{N_T} = \psi_{N_T} = 0 & \text{at } x = x_{N_T}; \end{cases} \tag{53}$$

$$\text{Hinged}: \begin{cases} u_1 = w_1 = 0,\ B_{11}\sum_{j=1}^{N_1} C_{1j}^{(1)}U_j + D_{11}\sum_{j=1}^{N_1} C_{1j}^{(1)}\psi_j = 0 & \text{at } x = x_1, \\ u_{N_T} = w_{N_T} = 0,\ B_{11}\sum_{j=N_1+1}^{N_T} C_{Nj}^{(1)}U_j + D_{11}\sum_{j=N_1+1}^{N_T} C_{Nj}^{(1)}\psi_j = 0 & \text{at } x = x_{N_T}; \end{cases} \tag{54}$$

$$\text{Free}: \begin{cases} A_{11}\sum_{j=1}^{N_1} C_{1j}^{(1)}U_j + B_{11}\sum_{j=1}^{N_1} C_{1j}^{(1)}\psi_j = 0,\ A_{55}\left(\sum_{j=1}^{N_1} C_{1j}^{(1)}W_j + \psi_1\right) = 0, & \\ B_{11}\sum_{j=1}^{N_1} C_{1j}^{(1)}U_j + D_{11}\sum_{j=1}^{N_1} C_{1j}^{(1)}\psi_j = 0 & \text{at } x = x_1, \\ A_{11}\sum_{j=N_1+1}^{N_T} C_{Nj}^{(1)}U_j + B_{11}\sum_{j=N_1+1}^{N_T} C_{Nj}^{(1)}\psi_j = 0,\ A_{55}\left(\sum_{j=N_1+1}^{N_T} C_{Nj}^{(1)}W_j + \psi_{N_T}\right) = 0, & \\ B_{11}\sum_{j=N_1+1}^{N_T} C_{Nj}^{(1)}U_j + D_{11}\sum_{j=N_1+1}^{N_T} C_{Nj}^{(1)}\psi_j = 0 & \text{at } x = x_{N_T}. \end{cases} \tag{55}$$

In addition, the interface defines the common boundary of the fluid and air subdomains, at which the governing equations (47)-(50) and (51)-(53) should be satisfied simultaneously. This requires the displacements and stresses to be equal at the interface ($x = x_{N1}, x_{N1+1}$):

$$\begin{cases} U_{N_1} = U_{N_1+1},\ W_{N_1} = W_{N_1+1},\ \psi_{N_1} = \psi_{N_1+1}; \\ A_{11}\sum_{j=1}^{N_1} C_{N_1j}^{(1)}U_j + B_{11}\sum_{j=1}^{N_1} C_{N_1j}^{(1)}\psi_j = A_{11}\sum_{j=N_1+1}^{N_T} C_{(N_1+1)j}^{(1)}U_j + B_{11}\sum_{j=N_1+1}^{N_T} C_{(N_1+1)j}^{(1)}\psi_j, \\ A_{55}\left(\sum_{j=1}^{N_1} C_{N_1j}^{(1)}W_j + \psi_{N_1}\right) = A_{55}\left(\sum_{j=N_1+1}^{N_T} C_{(N_1+1)j}^{(1)}W_j + \psi_{N_1+1}\right), \\ B_{11}\sum_{j=1}^{N_1} C_{N_1j}^{(1)}U_j + D_{11}\sum_{j=1}^{N_1} C_{N_1j}^{(1)}\psi_j = B_{11}\sum_{j=N_1+1}^{N_T} C_{(N_1+1)j}^{(1)}U_j + D_{11}\sum_{j=N_1+1}^{N_T} C_{(N_1+1)j}^{(1)}\psi_j. \end{cases} \tag{56}$$

Substituting the boundary conditions from Eqs. (53)-(55) and the compatibility conditions (56) into the governing equations (47)-(52) leads to a matrix system of algebraic equations as.

$$(\mathbf{M} + \mathbf{M}_F)\ddot{\mathbf{d}} + \mathbf{K}\mathbf{d} = \mathbf{0} \tag{57}$$

where $\mathbf{d} = \{\{u_i\}, \{w_i\}, \{\varphi_i\}\}^T$ ($i = 1, 2, \ldots, N$). $\mathbf{M}$ and $\mathbf{K}$ are the mass matrix and stiffness matrix, respectively. $\mathbf{M}_F$ is the added mass matrix due to the beam-fluid interaction. Among those, elements in $\mathbf{M}$ and $\mathbf{K}$ are constant associated with material and geometric parameters, while those in $\mathbf{M}_F$ are functions of unknow displacements. For the free vibration analysis, the displacement vector $\mathbf{d}$ takes the form of

$$\mathbf{d} = \mathbf{d}^* e^{i\Omega t} \tag{58}$$

in which $\mathbf{d}^*$ denotes the vibration mode vector, and Ω is the natural frequency. Substitution of Eq. (58) into Eq. (57) gives an eigenvalue equation as

$$\left[\mathbf{K} - \Omega^2(\mathbf{M} + \mathbf{M}_F)\right]\mathbf{d}^* = \mathbf{0} \tag{59}$$

As the values of elements in $\mathbf{M}_F$ are dependent on the displacements, an iterative procedure is used here to determine natural frequencies of the beam-fluid interaction system, with the iterative steps as follows:

(1) An initial eigenvalue (vibration frequency) and its associated eigenvector (vibration mode) of the FG-GPLRC beam in air are obtained from eigenvalue equation (59) with the added mass matrix $\mathbf{M}_F$ neglected.
(2) Using the eigenvector from step (1) to calculate $\mathbf{M}_F$, new eigenvalue and eigenvector are obtained from the updated eigenvalue equation (59).
(3) Step (2) continues until the relative error between the eigenvalues obtained from two consecutive iterations is<0.1%, then natural frequencies of the beam-fluid system can be obtained.

4. Results and discussion

In the following sections, comparison and parametric studies are

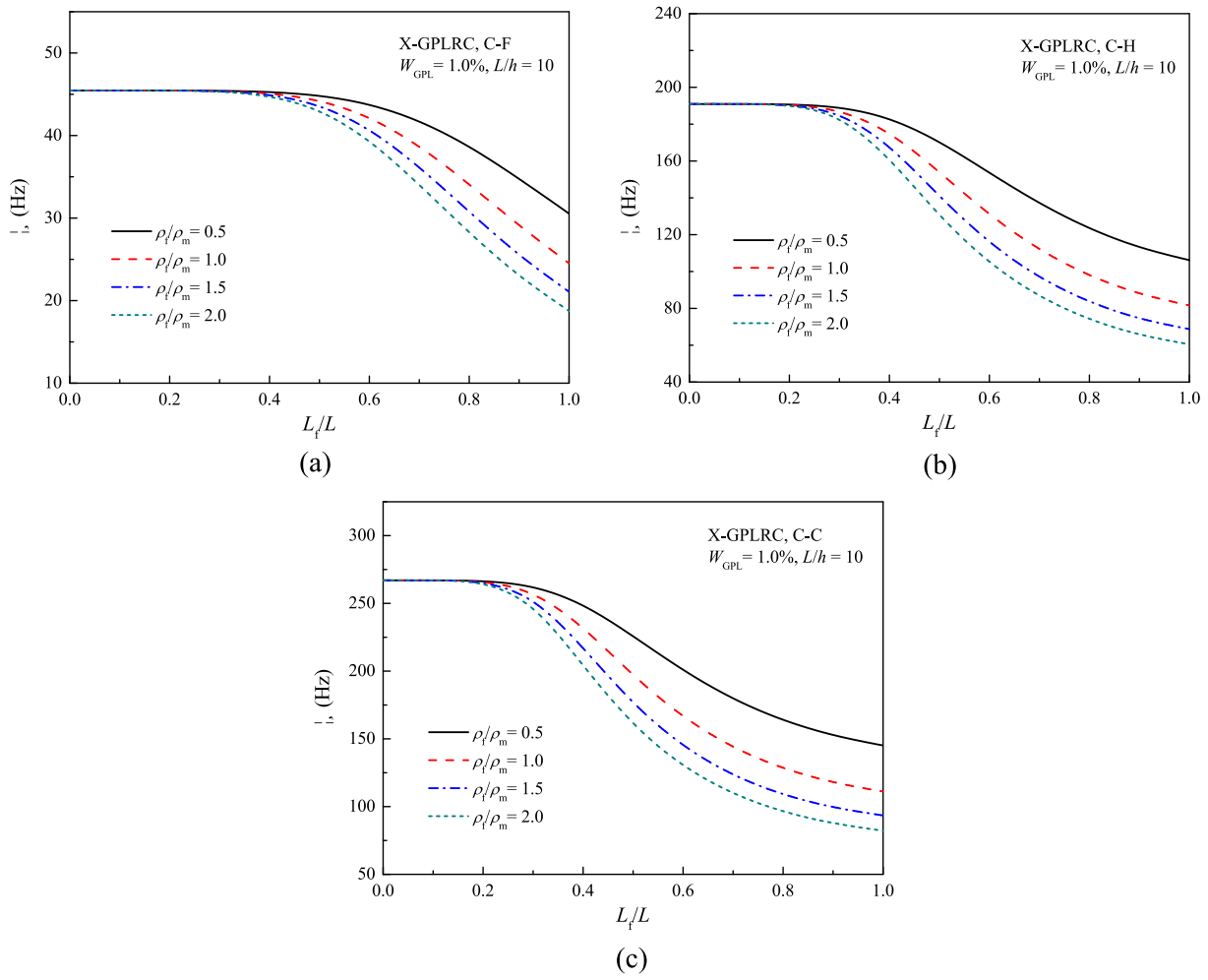

Fig. 11. Effect of fluid density on the fundamental frequency of FG-GPLRC beam-fluid interaction systems: (a) C-F; (b) C-H; (c) C-C.

conducted in order to supply information on the free vibration of FG-GPLRC beams in partially contact with fluid. FG-GPLRC beams are made from a mixture of epoxy and GPLs, and their material properties are as follows: $E_m = 3.0$ GPa, $\rho_m = 1200$ kg/m^3, $\nu_m = 0.34$; $E_{GPL} = 1.01$ TPa, $\rho_{GPL} = 1062.5$ kg/m^3, $\nu_{GPL} = 0.186$, $d_{GPL} = 1$ μm, $t_{GPL} = 1$ nm.

4.1. Convergence and comparison

Prior to parametric studies, convergence and comparison analyses are performed to validate the accuracy of the present formulation and solution procedure. Table 1 tabulates the fundamental frequencies of an X-GPLRC beam-fluid interaction system with varying number of grid points. In this example, $L_f/L = 0$ means that the beam is in air, while $L_f/L = 0.5$ and 1.0 represents that the beam is half and fully in contact with fluid, respectively. For simplicity, same number of grid points is selected for the fluid and air subdomains, namely $N_1 = N_2 = N$. It is shown that the present solutions are well convergent when the number of grid points is increased to 11. In addition, previous studies [19,23] have shown that a multilayer GPLRC beam/plate with 10 layers is sufficient to approximate an idea functionally graded beam/plate with smooth variation in material properties. Hence, $N_L = 10$ and $N = 10$ are used in all the subsequent numerical examples.

Fundamental frequency parameters of functionally graded carbon nanotube-reinforced composite (FG-CNTRC) beams in air are computed and compared in Table 2 with those of Wu *et al.* [50] using Ritz method, in which V^*_{cn} is the total volume fraction of CNTs; I_{10} and A_{110} are the values of I_1 and A_{11}, respectively, of a homogeneous beam made from the pure matrix material. Material properties used in this example can be found in the reference. In addition, fundamental frequency results of an isotropic homogeneous beam-water interaction system are listed and compared in Table 3 with those of Xing *et al.* [51] and Eftekhari and Jafari [52]. In this calculation, the elastic modulus of the beam is $E = 29.4$ GPa; the densities of the beam and water are $\rho_s = 2.4 \times 10^3$ kg/m^3 and $\rho_f = 1.0 \times 10^3$ kg/m^3, respectively. Comparison studies indicate that our results are in perfect agreement with those reported in the literature. Table 3 shows that the present solutions are slightly lower than the existing ones, this is because by using the classical beam theory the transverse shear deformation was neglected in the literature.

4.2. Parametric studies

In this section, parametric studies are conducted and comprehensive numerical results are provided to evaluate the influences of various parameters on free vibration behaviour of FG-GPLRC beam-fluid interaction systems, such as GPL distribution pattern, weight fraction and dimension, fluid density and depth, beam geometry, and boundary conditions. Unless otherwise stated, tabular and graphical results are presented for the X-GPLRC beam-fluid interaction system with $L/h = 10$ ($h = 0.1$ m), $W_{GPL} = 1.0\%$, $d_{GPL}/t_{GPL} = 1000$, and $\rho_f = 1000$ kg/m^3.

Table 4 tabulates the fundamental frequencies of cantilever FG-GPLRC beams in air and fully in contact with fluid. Four distribution patterns of GPLs are considered in this case, among which pattern X gives the highest fundamental frequency, followed by the patterns U, A, and O. Also, the fundamental frequency gradually increases as the GPL

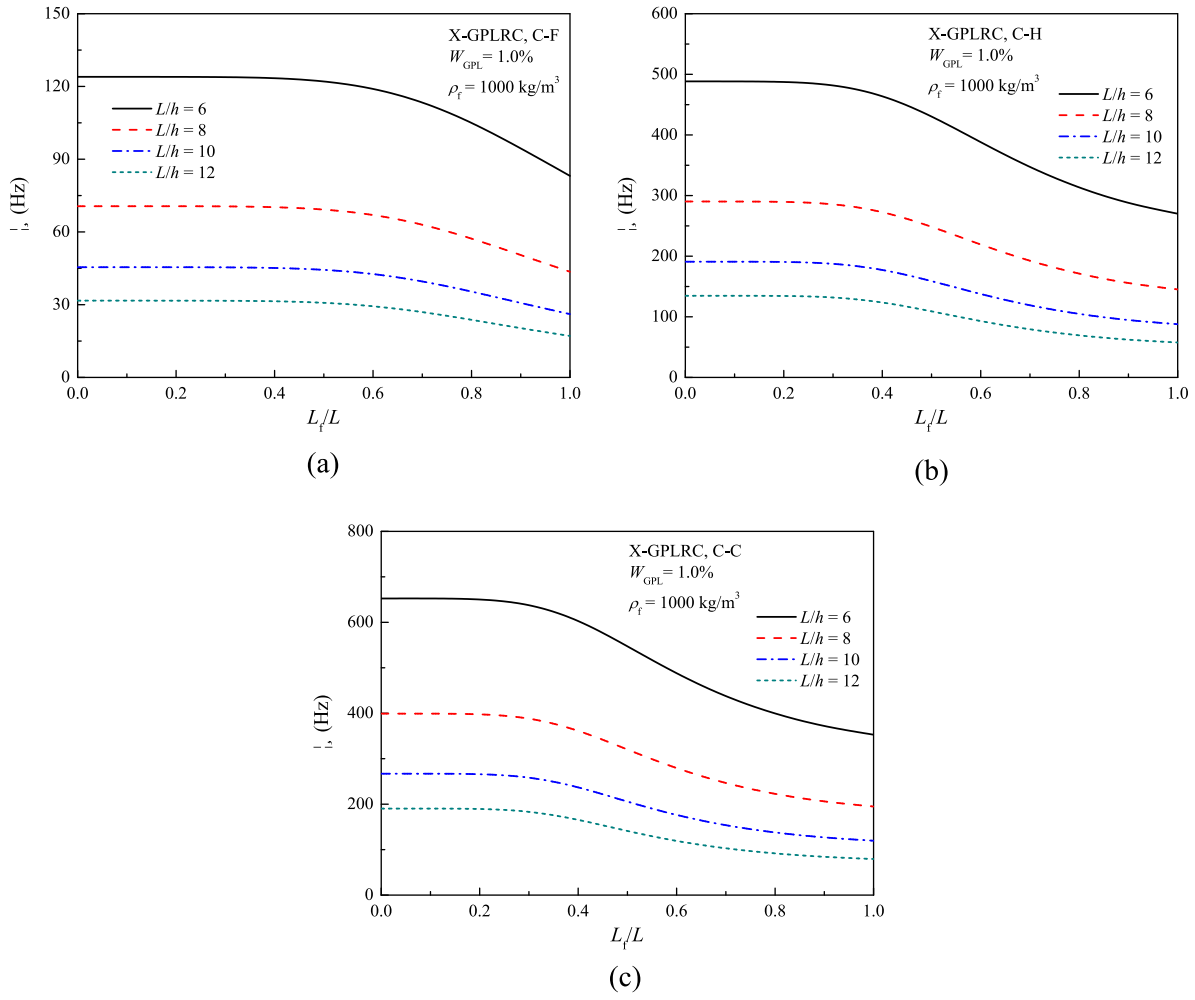

Fig. 12. Effect of slenderness ratio on the fundamental frequency of FG-GPLRC beam-fluid interaction systems: (a) C-F; (b) C-H; (c) C-C.

weight fraction rises. This is due to the fact that dispersing more reinforcements in the surface layers results in a higher beam stiffness. Compared with the results of the beam in air, the fundamental frequencies of the beam-fluid system are significantly decreased. The decrease percentages defined by $(\Omega^a - \Omega^f)/\Omega^a \times 100\%$ are depicted in Fig. 4, where Ω^a and Ω^f denote natural frequencies of the beams in air and in contact with fluid, respectively. It is seen that the decrease percentage remains nearly constant (~42.5%) for different GPL distribution patterns and weight fractions. This can be explained by the governing equation (59) in which the added mass matrix $\mathbf{M}_F$ characterising the beam-fluid interaction is independent of GPL parameters.

Table 5 gives the first three natural frequencies of X-GPLRC beams with different boundary conditions in air and fully in contact with fluid. The results show that the beam-fluid interaction declines the natural frequencies, and this effect is most pronounced for the first order frequency (Ω_1), then the second (Ω_2) and third (Ω_3) ones. For example, the first three frequencies of the C-H beam-fluid system are decreased by 54.0%, 38.1%, and 29.3% in sequence. Fig. 5 plots the decrease percentages of first three natural frequencies for different boundary conditions and shows that the decrease percentage of Ω_1 is largest for the C-C end support, followed by the C-H and C-F. However, this is inversed for Ω_3 that is most decreased for the C-F end support, then the C-H and C-C. As expected, the rigid end support (C-C) generates greater stiffness and thus brings about higher natural frequencies than those soft ones (C-H and C-F).

The influence of fluid on the free vibration is further investigated in Fig. 6 by comparing the vibration mode shapes of cantilever X-GPLRC beams in air and fully in contact with fluid. As can be seen, the fundamental vibration modes of the beam in air and the interaction system almost overlap, but the difference becomes more obvious for higher vibration modes. This is contrary to the observations in frequency analysis that the difference is most remarkable for the fundamental frequency, but gets reduced for higher order frequencies. The normalized hydrodynamic pressures corresponding to the first three vibration modes are evaluated using Eq. (23) and displayed in Fig. 7. It is observed that the higher order hydrodynamic pressure shows a more fluctuant mode shape.

We next investigate the free vibration of FG-GPLRC beams partially in contact with fluid. Numerical results, in terms of fundamental frequency Ω plotted against the dimensionless fluid depth L_f/L, are presented in Figs. 8-12 for the beam-fluid interaction systems with various parameters.

Figs. 8 and 9 depict the effects of GPL distribution pattern and weight fraction on the fundamental frequency versus the fluid depth curve, respectively. The results indicate that the frequency curves are increased by loading more GPLs in pattern X. The fundamental frequency of the C-F beam is slightly reduced as the fluid depth L_f/L changes from 0 to 0.4, beyond which the frequency is dramatically declined. The reason is that increasing the fluid depth leads to a higher hydrodynamic pressure, and then reduces the natural frequency. The curves of C-H and C-C beams show a similar trend with that of the C-F beam when L_f/L is lower than a certain value (~0.6 in Fig. 8), whereafter the effect of fluid depth becomes less significant again. In other words, the influence of fluid depth is remarkably reduced when the fluid surface approaches to the rigid

end supports (clamped and hinged). This is owing to the fact that near the beam ends the stiffness is enhanced by the rigid end supports, and therefore the effect of fluid is considerably weakened. This is also confirmed in Figs. 10-12.

Figs. 10 and 11 plot the effects of GPL diameter-to-thickness ratio and fluid density on the fundamental frequency of X-GPLRC beam-fluid systems, respectively. A greater value of d_{GPL}/t_{GPL} means that each individual GPL has a larger surface area (keeping t_{GPL} constant) or contains fewer monolayer graphene sheets (keeping d_{GPL} constant). Fig. 10 shows that the fundamental frequency is raised with an increase of d_{GPL}/t_{GPL}, but this influence tends to be much less pronounced as the value of d_{GPL}/t_{GPL} further rises. Fig. 11 indicates that the frequency curves for different fluid densities are almost identical when the fluid depth $L_f/L < 0.4$ for the C-F beam, and $L_f/L < 0.2$ for the C-H and C-C beams, beyond which the frequency curves are lowered as the fluid density increases. This is because a higher fluid density enlarges the values of elements (I_f) in the added mass matrix $\mathbf{M}_F$, and consequently reduces the natural frequency.

Fig. 12 investigates the influence of slenderness ratio on the fundamental frequency versus fluid depth curves and four cases of $L/h = 6$, 8, 10, 12 are considered here. A larger slenderness ratio weakens the beam stiffness, and accordingly reduces the fundamental frequency. In addition, the frequency curves become less steep as the slenderness ratio increases, implying that a greater slenderness ratio diminishes the effect of fluid depth on the fundamental frequency.

5. Conclusion

The free vibration of FG-GPLRC beams partially in contact with fluid has been investigated within the framework of FSDT and Hamilton's principle. The 3D Halpin-Tsai model is introduced to estimate the elastic modulus of graphene nanocomposites. The fluid velocity potential is obtained by using the method of variable separation. Governing equations of free vibration are discretised by the multidomain GDQ approach and then solved by a standard iteration procedure. Tabular and graphical results are presented to illustrate the influences of GPL distribution pattern, concentration and dimension, fluid depth and density, beam geometry, as well as boundary conditions on the free vibration characteristics of FG-GPLRC beam-fluid interaction systems. The main findings are concluded as follows:

(1) By considering the 3D-randomly oriented GPLs, the 3D Halpin-Tsai model gives a reasonable estimation of the elastic modulus of graphene nanocomposites.
(2) Compared to the beam in air, the natural frequencies of the beam fully in contact with fluid are significantly decreased, but the decrease percentage remains constant for different GPL distribution patterns and weight fractions.
(3) The beam-fluid interaction reduces the fundamental frequency most, but it hardly affects the first order vibration mode shape. Also, the fundamental frequency declines as the fluid depth increases; however, this effect is considerably weakened when the fluid surface is close to the rigid end supports of the beam.
(4) The fundamental frequency of the interaction system grows with an increase of GPL diameter-to-thickness ratio, yet this influence becomes much less pronounced as d_{GPL}/t_{GPL} further increases.
(5) A larger fluid density leads to a greater added mass and results in a lower fundamental frequency, but this effect can be neglected when the fluid depth is small.

Data Availability

The raw/processed data required to reproduce these findings cannot be shared at this time as the data also forms part of an ongoing study.

CRediT authorship contribution statement

Helong Wu: Conceptualization, Methodology, Formal analysis, Writing – original draft. **Yilin Li:** Investigation, Visualization. **Long Li:** Software, Validation. **Sritawat Kitipornchai:** Supervision. **Lin Wang:** Methodology, Writing – review & editing. **Jie Yang:** Conceptualization, Writing – review & editing.

Declaration of Competing Interest

The authors declare that they have no known competing financial interests or personal relationships that could have appeared to influence the work reported in this paper.

Acknowledgements

The work described in this paper was supported by the National Natural Science Foundation of China (Grant No. 11902290). The authors are grateful for this financial support.

References

[1] Akinwande D, Brennan CJ, Bunch JS, Egberts P, Felts JR, Gao H, et al. A review on mechanics and mechanical properties of 2D materials—Graphene and beyond. Extreme Mech Lett 2017;13:42–77.
[2] Balandin AA, Ghosh S, Bao W, Calizo I, Teweldebrhan D, Miao F, et al. Superior thermal conductivity of single-layer graphene. Nano Lett 2008;8(3):902–7.
[3] Bonaccorso F, Colombo L, Yu G, Stoller M, Tozzini V, Ferrari AC, et al. Graphene, related two-dimensional crystals, and hybrid systems for energy conversion and storage. Science 2015;347(6217):1246501.
[4] Lee C, Wei X, Kysar JW, Hone J. Measurement of the elastic properties and intrinsic strength of monolayer graphene. Science 2008;321(5887):385–8.
[5] Ji X-Y, Cao Y-P, Feng X-Q. Micromechanics prediction of the effective elastic moduli of graphene sheet-reinforced polymer nanocomposites. Model Simul Mater Sc 2010;18(4):045005.
[6] Young RJ, Kinloch IA, Gong L, Novoselov KS. The mechanics of graphene nanocomposites: A review. Compos Sci Technol 2012;72(12):1459–76.
[7] Papageorgiou DG, Kinloch IA, Young RJ. Mechanical properties of graphene and graphene-based nanocomposites. Prog Mater Sci 2017;90:75–127.
[8] Ponnamma D, Yin Y, Salim N, Parameswaranpillai J, Thomas S, Hameed N. Recent progress and multifunctional applications of 3D printed graphene nanocomposites. Compos Part B-Eng 2021;204:108493.
[9] Das TK, Prusty S. Graphene-based polymer composites and their applications. Polym-Plast Technol 2013;52(4):319–31.
[10] Wu H, Wang J, Kang X, Wang C, Wang D, Liu J, et al. Glucose biosensor based on immobilization of glucose oxidase in platinum nanoparticles/graphene/chitosan nanocomposite film. Talanta 2009;80(1):403–6.
[11] Wu Q, Xu Y, Yao Z, Liu A, Shi G. Supercapacitors based on flexible graphene/polyaniline nanofiber composite films. ACS Nano 2010;4(4):1963–70.
[12] Rafiee MA, Rafiee J, Yu Z-Z, Koratkar N. Buckling resistant graphene nanocomposites. Appl Phys Lett 2009;95(22):223103.
[13] Barretta R, Luciano R. Analogies between Kirchhoff plates and functionally graded Saint-Venant beams under torsion. Continuum Mech Therm 2015;27(3):499–505.
[14] Barretta R, Feo L, Luciano R. Some closed-form solutions of functionally graded beams undergoing nonuniform torsion. Compos Struct 2015;123:132–6.
[15] Apuzzo A, Barretta R, Faghidian SA, Luciano R, De Sciarra FM. Nonlocal strain gradient exact solutions for functionally graded inflected nano-beams. Compos Part B-Eng 2019;164:667–74.
[16] Yang J, Wu H, Kitipornchai S. Buckling and postbuckling of functionally graded multilayer graphene platelet-reinforced composite beams. Compos Struct 2017;161:111–8.
[17] Feng C, Kitipornchai S, Yang J. Nonlinear bending of polymer nanocomposite beams reinforced with non-uniformly distributed graphene platelets (GPLs). Compos Part B-Eng 2017;110:132–40.
[18] Song M, Kitipornchai S, Yang J. Free and forced vibrations of functionally graded polymer composite plates reinforced with graphene nanoplatelets. Compos Struct 2017;159:579–88.
[19] Wu H, Yang J, Kitipornchai S. Dynamic instability of functionally graded multilayer graphene nanocomposite beams in thermal environment. Compos Struct 2017;162:244–54.
[20] Yang Z, Liu A, Lai S-K, Safaei B, Lv J, Huang Y, et al. Thermally induced instability on asymmetric buckling analysis of pinned-fixed FG-GPLRC arches. Eng Struct 2022;250:113243.
[21] Shen H-S, Lin F, Xiang Y. Nonlinear bending and thermal postbuckling of functionally graded graphene-reinforced composite laminated beams resting on elastic foundations. Eng Struct 2017;140:89–97.
[22] Wang Y, Feng C, Wang X, Zhao Z, Romero CS, Dong Y, et al. Nonlinear static and dynamic responses of graphene platelets reinforced composite beam with dielectric permittivity. Appl Math Model 2019;71:298–315.

[23] Wu H, Kitipornchai S, Yang J. Thermal buckling and postbuckling of functionally graded graphene nanocomposite plates. Mater Design 2017;132:430–41.
[24] Wu H, Yang J, Kitipornchai S. Parametric instability of thermo-mechanically loaded functionally graded graphene reinforced nanocomposite plates. Int J Mech Sci 2018;135:431–40.
[25] Wu H, Zhu J, Kitipornchai S, Wang Q, Ke L-L, Yang J. Large amplitude vibration of functionally graded graphene nanocomposite annular plates in thermal environments. Compos Struct 2020;239:112047.
[26] Shen H-S, Xiang Y, Fan Y. Nonlinear vibration of functionally graded graphene-reinforced composite laminated cylindrical shells in thermal environments. Compos Struct 2017;182:447–56.
[27] Dong YH, Zhu B, Wang Y, He LW, Li YH, Yang J. Analytical prediction of the impact response of graphene reinforced spinning cylindrical shells under axial and thermal loads. Appl Math Model 2019;71:331–48.
[28] Zhao S, Zhao Z, Yang Z, Ke LiaoLiang, Kitipornchai S, Yang J. Functionally graded graphene reinforced composite structures: A review. Eng Struct 2020;210:110339.
[29] Feng C, Kitipornchai S, Yang J. Nonlinear free vibration of functionally graded polymer composite beams reinforced with graphene nanoplatelets (GPLs). Eng Struct 2017;140:110–9.
[30] Song M, Gong Y, Yang J, Zhu W, Kitipornchai S. Nonlinear free vibration of cracked functionally graded graphene platelet-reinforced nanocomposite beams in thermal environments. J Sound Vib 2020;468:115115.
[31] Wang M, Xu Y-G, Qiao P, Li Z-M. A two-dimensional elasticity model for bending and free vibration analysis of laminated graphene-reinforced composite beams. Compos Struct 2019;211:364–75.
[32] Shen HS, Lin F, Xiang Y. Nonlinear vibration of functionally graded graphene-reinforced composite laminated beams resting on elastic foundations in thermal environments. Nonlinear Dynam 2017;90(2):899–914.
[33] Shen H-S, Xiang Y, Lin F. Nonlinear vibration of functionally graded graphene-reinforced composite laminated plates in thermal environments. Comput Method Appl M 2017;319:175–93.
[34] Kiani Y. Isogeometric large amplitude free vibration of graphene reinforced laminated plates in thermal environment using NURBS formulation. Comput Method Appl M 2018;332:86–101.
[35] Muni Rami Reddy R, Karunasena W, Lokuge W. Free vibration of functionally graded-GPL reinforced composite plates with different boundary conditions. Aerosp Sci Technol 2018;78:147–56.
[36] Qaderi S, Ebrahimi F, Mahesh V. Free vibration analysis of graphene platelets–reinforced composites plates in thermal environment based on higher-order shear deformation plate theory. Int J Aeronaut Space 2019;20(4):902–12.
[37] Khorshidi K, Bakhsheshy A. Free vibration analysis of a functionally graded rectangular plate in contact with a bounded fluid. Acta Mech 2015;226(10):3401–23.
[38] Shahbaztabar A, Ranji AR. Free vibration analysis of functionally graded plates on two-parameter elastic supports and in contact with stationary fluid. J Offshore Mech Arct 2017;140(2).
[39] Li H-C, Ke L-L, Yang J, Kitipornchai S, Wang Y-S. Free vibration of variable thickness FGM beam submerged in fluid. Compos Struct 2020;233:111582.
[40] Houmat A. Three-dimensional free bending vibrations of variable radius functionally graded circular column immersed in infinite fluid. Eng Struct 2021;249:113351.
[41] Thinh TI, Tu TM, Van Long N. Free vibration of a horizontal functionally graded rectangular plate submerged in fluid medium. Ocean Eng 2020;216:107593.
[42] Halpin J, Kardos J. The Halpin-Tsai equations: a review. Polym Eng Sci 1976;16(5):344–52.
[43] Van Es MA, *Polymer-clay nanocomposites: the importance of particle dimensions*. 2001, Delft University of Technology.
[44] Hull D. An Introduction to Composite Materials. Cambridge University Press; 1981.
[45] Harris B. Engineering Composite Materials. London: Institute of metals; 1986.
[46] Zhao X, Zhang Q, Chen D, Lu P. Enhanced mechanical properties of graphene-based poly (vinyl alcohol) composites. Macromolecules 2010;43(5):2357–63.
[47] Shu C, *Generalized differential-integral quadrature and application to the simulation of incompressible viscous flows including parallel computation*. 1991, University of Glasgow (United Kingdom).
[48] Shu C, Richards BE. Application of generalized differential quadrature to solve two-dimensional incompressible Navier-Stokes equations. Int J Numer Meth Fl 1992;15(7):791–8.
[49] Shu C, Chew Y. Application of multi-domain GDQ method to analysis of waveguides with rectangular boundaries. Prog Electromagn Res 1999;21:1–19.
[50] Wu HL, Yang J, Kitipornchai S. Nonlinear vibration of functionally graded carbon nanotube-reinforced composite beams with geometric imperfections. Compos Part B-Eng 2016;90:86–96.
[51] Xing JT, Price WG, Pomfret MJ, Yam LH. Natural vibration of a beam—water interaction system. J Sound Vib 1997;199(3):491–512.
[52] Eftekhari SA, Jafari AA. A mixed modal-differential quadrature method for free and forced vibration of beams in contact with fluid. Meccanica 2014;49(3):535–64.